Direct Thrust Measurements of a circular waveguide Electron Cyclotron Resonance Thruster

IEPC-2022-487

Presented at the 37th International Electric Propulsion Conference
Massachusetts Institute of Technology, Cambridge, MA, USA
June 19-23, 2022

Inchingolo M. R. [1], Merino M.[2] and Navarro-Cavallé J.[3]
Equipo de Propulsión Espacial y Plasmas, Universidad Carlos III de Madrid, Leganés, Madrid, 28911, Spain

Direct thrust measurements are performed on a waveguide-based electrodeless ECR thruster working at the 5.8 GHz microwave frequency using an amplified displacement pendulum thrust balance. Thrust levels between 1–3.5 **mN were found for power levels in the range of** 50–350 **W for the cases of 2 and 4 sccm of Xenon propellant mass flow rate. The thrust efficiency was found to be 2 and 5 %. Plasma probes such as a Faraday cup, Langmuir Probe and Retarding Potential Analyser, are used as well to assess partial efficiencies. Results suggest the presence of a population of fast electrons with energies up to about 300 eV.**

I. Introduction

Electrodeless plasma thrusters [1] promise more simplicity and longer lifetimes with respect to plasma thrusters using electrodes which are subject to erosion and performance degradation. On the other hand this thruster class typically suffers lower I_{sp} and thrust efficiency, and higher plume divergence, when compared with Hall thrusters and Ion Thrusters, critical parameters for emerging from the prototype state to real-life integration on a satellite.

A recent trend in this context has been brought by the developments on coaxial ECR thrusters (ECRT) under research at the ONERA National French Aerospace Laboratory [2–5]. Promising and competitive propulsive performance were reported, with thrust efficiencies approaching the 30–50% range [3, 6]. However, the coaxial ECR thruster design, suffers from erosion of the central conductor and metallic deposition on the thruster backplate [4, 5], which would limit again the lifetime and partially invalidate the benefits of having an electrodeless design.

The working principle of an ECRT relies on the electron cyclotron resonance to couple electromagnetic power to the plasma electrons. This resonance happens where the relation $\omega_{ce} = \omega$ is satisfied, being $\omega_{ce} = eB/m_e$ the electron cyclotron angular frequency and ω the applied electromagnetic wave angular frequency [7, 8], typically in the range of microwaves. The ECR heats up the electrons. Part of the coupled power is spent on sustaining ionization, and ideally, the remaining part should be transformed into plasma kinetic energy, but a considerable fraction is inefficiently lost on plasma-wall recombination and excitation losses. The conversion of electron thermal energy into ion kinetic power is achieved by expanding the plasma along a magnetic nozzle, i.e. an external divergent magnetic field [9, 10]. Plasma expansion through the MN is quasi-neutral and current free, and thus neutralizers are not needed.

The microwave-plasma coupling is design-dependent, and apart from the mentioned coaxial ECRT, circular waveguides can also be used with the possible advantage of having the central conductor removed. However, waveguide ECRTs were investigated in the 1960s [11–13] and 1990s [14–16], showing low propulsive performances in the 1-5% thrust efficiency range.

In order to further investigate the physics of waveguide ECRTs, optimize their operation, and identify the limitations of this technology, experiments are being carried out at the plasma and space propulsion laboratory (EP2) on a newly designed waveguide ECRT [17, 18]. A schematic view of the thruster here presented is shown in figure 1. It is composed of a central circular waveguide constituting the plasma chamber; a radially magnetised ring magnet is responsible for the creation of the magnetic field necessary for the resonance,and a coil is used for trimming/tuning the magnetic nozzle

[1]PhD candidate, Departamento de Bioingeniería e Ingeniería Aeroespacial, minching@pa.uc3m.es
[2]Associate Professor, Departamento de Bioingeniería e Ingeniería Aeroespacial, mario.merino@uc3m.es.
[3]Visiting Professor, Departamento de Bioingeniería e Ingeniería Aeroespacial, janavarr@ing.uc3m.es

shape and resonance position. The microwave frequency used is 5.8 GHz, allowing for smaller waveguide dimensions than the usual 2.45 GHz frequency, and consequently lowerling the size of the device, and its mass flow rate and power requirements.

Thrust balance (TB) measurements on waveguide ECRTs were performed in the past by Crimi and Miller [13] on the Mark VA-S engine. Mercury propellant was used. The accuracy of the results was considered questionable because of difficulties in correctly measuring the propellant mass flow rate. Indirect measurements were performed instead by Sercel [16] showing results in the 2% thrust efficiency range. Only recently [5], Peterschmitt performed a comparison of direct thrust measurements between a coaxial geometry and a waveguide one. The tested waveguide thruster was designed with the same dimensions and operated at the same working point of the coaxial version. Results showed thrust efficiencies of 5% and 1% respectively for the coaxial and waveguide thrusters operating in the range of 10–50 W of deposited power regime for 1 sccm of Xenon propellant. However, the analysis left the possibility open that further optimization could be possible for the waveguide design.

In this work we present the first thrust balance measurements performed on the waveguide ECRT designed at EP2, and we relate them with the plasma plume properties measured with intrusive probes. The trends found serve as a baseline for future thruster design optimization.

The rest of the paper is organised as follows. In section II, first the ECRT, the thrust balance, the plasma probes and their assembly in the vacuum chamber are presented; secondly the procedures used for the thrust measurements and post-processing are outlined. In section III the thrust measurements are shown, insights on the results is provided by the use of intrusive diagnostics probing the expanding plasma. Finally, in section IV, the research carried out is discussed and the conclusions are drawn.

II. Experimental setup and methodologies

The waveguide Electron Cyclotron Resonance thruster prototype, object of this test campaign, is shown in figure 1 and its main design parameters are shown in table 1. Figure 1 displays, along the thruster axis, from left to right, the following items: the latest segment of the waveguide transmission line, the DC-block, the aluminium circular waveguide segment and the plasma discharge chamber (PC), made of stainless-steel.

The DC-block allows keeping the thruster (plasma discharge chamber) electrically floating with the respect to the transmission line and consists simply in two circular waveguides aligned, with a vacuum gap in between. Analysis with ANSYS Maxwell confirmed that only a negligible amount of power is lost through the gap (power dissipated <2% if gap distance <3mm). This design of the DC block is as well fundamental for thrust measurements since it enables the TB to displace while leaving the thruster electrically floating.

Continuing towards the right, the aluminium waveguide and the PC have the same inner diameter and are separated by a quartz window surrounded by a high temperature Perfluoroelastomer (FFKM) o-ring, which serves to avoid propellant leaks to the waveguide side.

The connection to the mounting plate is allowed by inserting the waveguide into an anodized aluminum cylinder (in yellow in Figure 1) and then securing it with a set-screw. This solution ensures that the thruster is well aligned respect to the magnetic field generator and electrically floating also with respect to the TB.

A permanent magnet and an electromagnet make up the magnetic field generator. The permanent magnet consists of a radially magnetized ring, which is made of 12 Sm-Co YXG-32 magnets glued together and enclosed in an aluminium box. Figure 2 depicts the magnetic field topology and strength generated by this magnet. The field it generates suffices to reach the ECR conditions inside the device. On the other hand, the electromagnet can be used to alter the shape of the magnetic nozzle and displace the resonance position. In this work, the thruster exit plane and center-line define the coordinate system as displayed in figure 1. Thus, the resonance can be displaced between $z = [-9, 0]$ mm when the electromagnet current is varied between $I_c = [0, 10]$ A respectively, at the same time the magnetic nozzle divergence is decreased for increasing currents. Although the electromagnet was kept mounted, the results shown in this paper are obtained with the permanent magnet only.

The propellant (Xe) is fed into the thruster chamber through a lateral threaded stainless steel tube, which is inserted in the injector (see figure 3) by the quartz backplate. In a previous work [18], a two-holes neutral injection scheme was used, but plume azimuthal inhomogeneities were observed. To correct for this effect, in this work the injector is a stainless steel component presenting two annular channels connected by a series of internal holes (which help equalizing the pressure within the ring), the gas is then fed into the PC by a second series of 12 radial holes of 1 mm in diameter. Axially, these holes are located at 2 mm downstream from the thruster backplate ($z = -18$ mm).

The mass flow rate is set and measured by a Bronkhorst EL-FLOW Select Xenon calibrated mass flow controller, with an accuracy of 0.1 sccm and 100 sccm full range. Previous experiments with a similar prototype [18] have shown that the thruster is able to ignite with a mass flow rate up to $\dot{m}_p$ = 40sccm, but better performances were found below 5 sccm, and for this reason the thrust measurements have focused in the low mass flow rate range.

The waveguide transmission line (TL) delivers the microwaves from the generator to the thruster. Figure 5a shows the scheme of the transmission line used to feed the thruster with microwaves. The microwave power is generated with a tunable power 5.8 GHz Magnetron (IBF GEN5800/0.8KW2CIA) with rectangular waveguide output WR159 (1), it includes an isolator (2) composed by a circulator and a dummy load. This is necessary to protect the magnetron from the reflected power. A dual directional coupler (IBF WR159DDC60NA) (3), with a directivity of 25 dB and a coupling factor of 60 dB, is used for forward and reflected power measurements using two independent power meters (Ladybug LB479A units). A stub tuner (4) is used to match the TL to the thruster impedance. Downstream, the air-vacuum interface (5) is realised with a pressure window (Muegge GA2604) mounted on a custom vacuum chamber flange. In the vacuum side, a flexible waveguide (Flexiguide)(6) eases the alignment with the rest of the thruster assembly and a rectangular to circular waveguide (Flann 14643)(7) transforms the TE01 mode of the rectangular waveguide to the the TE11 mode of the circular waveguide.

To prevent any potential leaks of microwave radiation to the laboratory, the vacuum chamber windows were covered with metallic grids; a microwave leak detector calibrated for the working frequency was constantly used to monitor the radiation level.

A distinction must be made between the Microwave Power set on the Microwave power supply P_{set} and the one delivered to the thruster. The two power meters connected to the dual directional coupler (3) provide as an output the forward power P_F and the reflected power P_R. The power delivered to the thruster can be estimated as $P_T = P_F\gamma^2 - \frac{P_R}{\gamma^2}$, where γ is the transmission coefficient (S12) of the transmission line in between the directional coupler and the thruster. The value of γ found for this specific TL with a calibrated VNA is $\gamma = 0.94$. The accuracy of the measurements of P_F, P_R and consequently P_T, strongly depends on the value of the measured reflection coefficient $R = \frac{P_R}{\gamma^4 P_F}$ and the directivity of the directional coupler [5, 19]. Keeping the value of reflections low is thus fundamental for an accurate estimation of the power delivered to the thruster. In this work the value of the reflection coefficient is kept below 6% by matching the transmission line at every thruster working point using the stub tuner (4). We estimate that the error on the power delivered to the thruster is below 15% for the tested working points.

In figure 5b shows a cut-view of the described assembly inside the vacuum chamber facility. The vacuum chamber consists of a 304-316 stainless-steel cylinder 3.5 m long, with an inner diameter of 1.5 m. The chamber is equipped with the following pumps: a dry mechanical pump Leyvac LV80 with pumping speed about 80 m^3/h, a pair of turbo-molecular pumps, Leybold MAGW2.200iP with 2000 l/s of pumping speed each, and three cryopanels, Leyvac 140 T-V. The total pumping speed is about 37,000 l/s for Xe, reaching an ultimate pressure of 10^{-7} mbar in dry conditions. This facility allows to keep an operational pressure between $2 \cdot 10^{-6} - 5 \cdot 10^{-6}$ mbar for a Xenon load of 1 to 4 sccm, being the pressure to gas load response quite linear.

In front of the thruster exit plane there is a polar probe positioning system, also shown in figure 5 (8). This system is capable of displacing the probes on a plane along the radial ρ and polar direction, indicated with α. The resolution of the system is 1° and 300μm for the polar and radial direction respectively. The center of rotation of the probe positioning system is aligned with the thruster exit plane. In addition to the thrust balance described below, in this work, also intrusive electrostatic probes are used: an RPA (Impedance-Semion single button probe) to assess for the ion energy in the far plume, a Faraday cup (FC) to measure the ion current profile and provide information on the utilization efficiency and plume divergence, a Langmuir Probe (LP) that provides properties such as the plasma density, potential, and electron temperature. Ref. [20] provides more information about the design of these last two probes. The data analysis and procedures of Ref. [21] are used to retrieve the plasma properties from the scanned data, i.e. I-V characteristic curve of a LP.

The LP was aligned with the thruster axis and used to scan the plume with 50 mm $< z <$ 400 mm. The FC instead scanned the plume on a plane at constant ρ = 350 mm varying α within $-\pi/2 < \alpha < \pi/2$. The RPA was aligned with the thruster axis and positioned at a distance of z = 350 mm.

Furthermore, the thruster discharge chamber floating potential was acquired during the overall test campaign.

The thruster axis is parallel to the vacuum chamber axis and is off-axis of about 100 mm. The thruster outlet section is about 2 m away from the chamber downstream wall, aiming to minimize the plume-chamber wall interaction. The thrust balance is mounted on a rail system positioned at the top internal part of the chamber.

As depicted in figure 1, at the top, the thruster is directly mounted on the TB with an interface designed so that its center of mass is as close as possible to thrust balance pendulum axis, this allows to exploit the full displacement range of the balance displacement sensor. In addition to the mechanical connection, only two electrical connections of the

Plasma Chamber Dimensions: Radius, Length	18mm, 20mm
Microwave Power	50-300 W
Mass flow rate (Xe)	1-40sccm
MW frequency	5.8 GHz
B resonance	2070 G
Magnet type	Sm-Co YXG-32
Max electromagnet power	350 W
Electromagnet max B field	450G

Table 1 ECRT design and operational parameters overview.

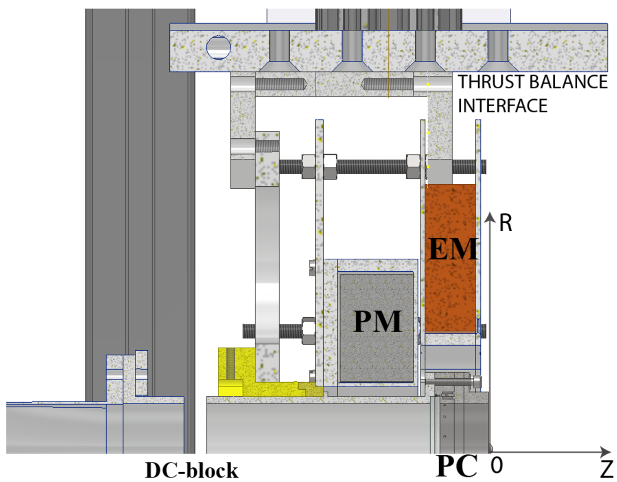

Fig. 1 CAD section representation of the thruster assembly.

thruster to the balance are necessary: the coil and the thruster floating potential cable. Since these cables would perturb the thrust measurements, the TB presents four galinstan liquid metal connectors which provide electrical continuity, with null friction, between the movable and fixed part of the TB assembly.

The complete setup of the thruster mounted on the thrust balance, is shown in figure 4. The thrust balance used for this work is deeply discussed in reference [22], for the sake of completeness, follows a short description. The TB is a modification of the Variable Amplitude Hanging Pendulum with Extended Range (VAHPER) design by Polzin et al. [23]. This design accounts for two arms, a vertical one on which the thruster is mounted and an horizontal one. The use of the second horizontal arm, coupled to the main vertical one with a pair of flexural pivots, leads to the mechanical amplification of the angular displacement of $31^o/^o$. The displacement is measured on this secondary arm for finer accuracy. At the cost of increased complexity, this design allows to have a shorter vertical arm respect to the simple pendulum approach, furthermore, the displacement measurement can be performed far from the thruster. As typically implemented in thrust balances for electric propulsion, an eddy current break is used to damp the balance oscillations that otherwise would continue indefinitely, this allows the balance to closely follow the thrust oscillations with a short settling time (about 2s). The displacement response of the TB is directly proportional to the thrust force. The proportionality constant depends on the mass distribution and thruster positioning on the balance, and it is provided by means of calibration. This TB implements two types of calibrations systems: a voice coil mounted on a load cell (refer to [22]) directly applying a force to the balance vertical arm, and a system involving pre-calibrated weights applied on an additional horizontal arm (refer to figure 4). In the case of permanent magnet thrusters, such as the one object of this work, the voice coil calibration system results are not suitable since the thruster PM magnetic field exerts a force on the voice coil magnet (mounted on the static part), thus affecting the force measurement. For these reasons, the weight calibration system was used.

A schematic representation of the weight calibration system is available in figure 6. The weights (fishing weights of $m_{cal} = 0.5$ gr) are loaded on a thin nylon wire ($\phi = 0.16$ mm) separated by a distance of 25 mm, one of its extremities is

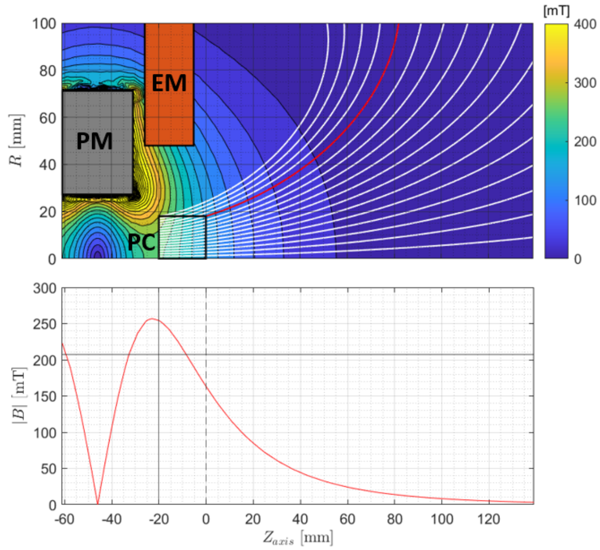

Fig. 2 (a) 2D plot and streamlines of the ECRT magnetic field. The streamline in red is the streamlines starting from the exit plane when the electromagnet current is: 0 A. (b) Magnitude of the on-axis magnetic field for the three electromagnet current cases. The horizontal line represents the resonance field. The solid black vertical line the backplate, and the dashed the exit-plane.

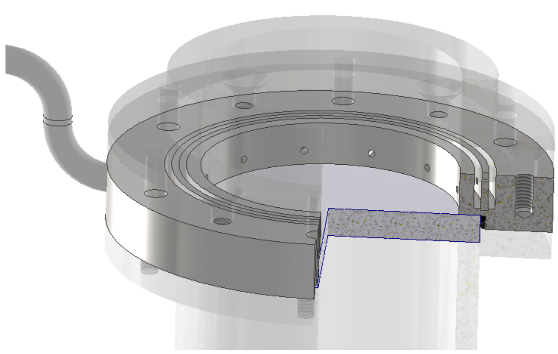

Fig. 3 CAD representation of the injector. A section view of the double internal ring channels is visible. The top stainless steel cover and the rest of the PC are shown as transparent. The quartz window and the FFKM o-ring are also visible.

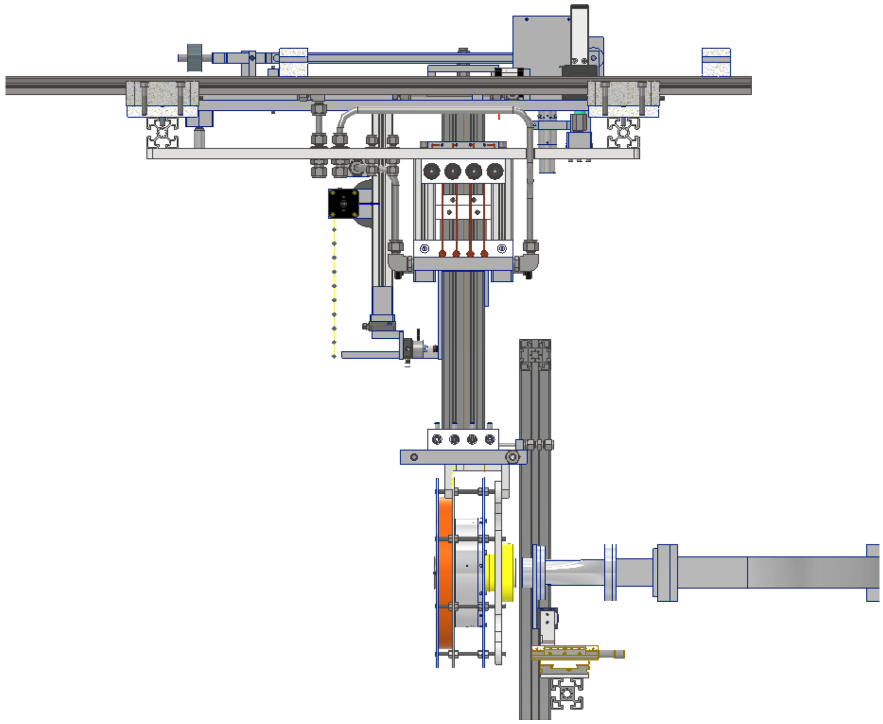

Fig. 4 ECR thruster and thrust balance assembly.

(a)

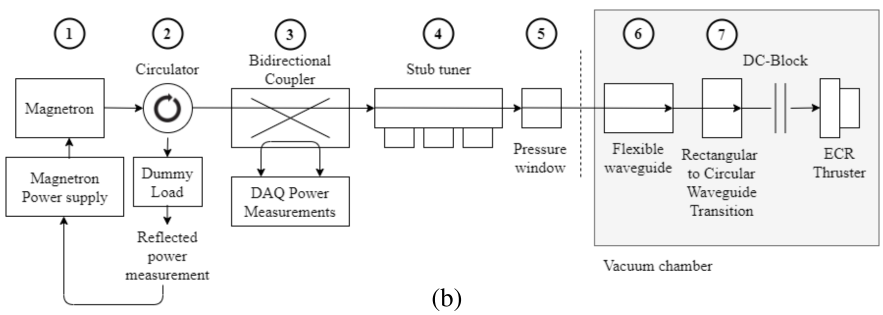

(b)

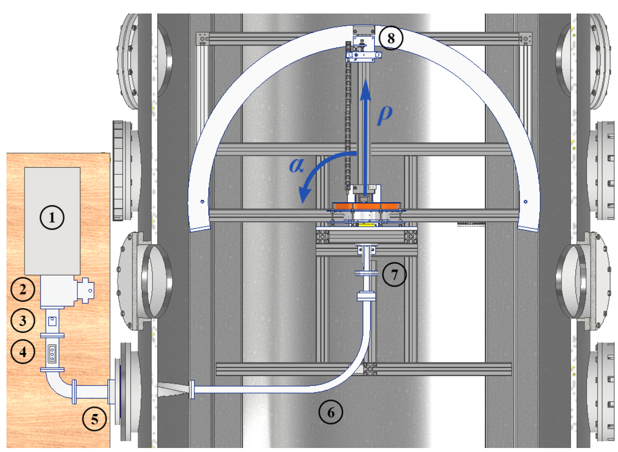

Fig. 5 (a) Scheme of the transmission line used during all the experiments. (b) Cut-view of the entire setup mounted in the EP2 large vacuum chamber facility.

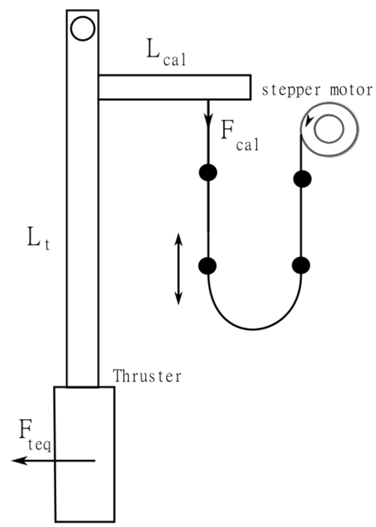

Fig. 6 Schematic representation of the weights calibration system.

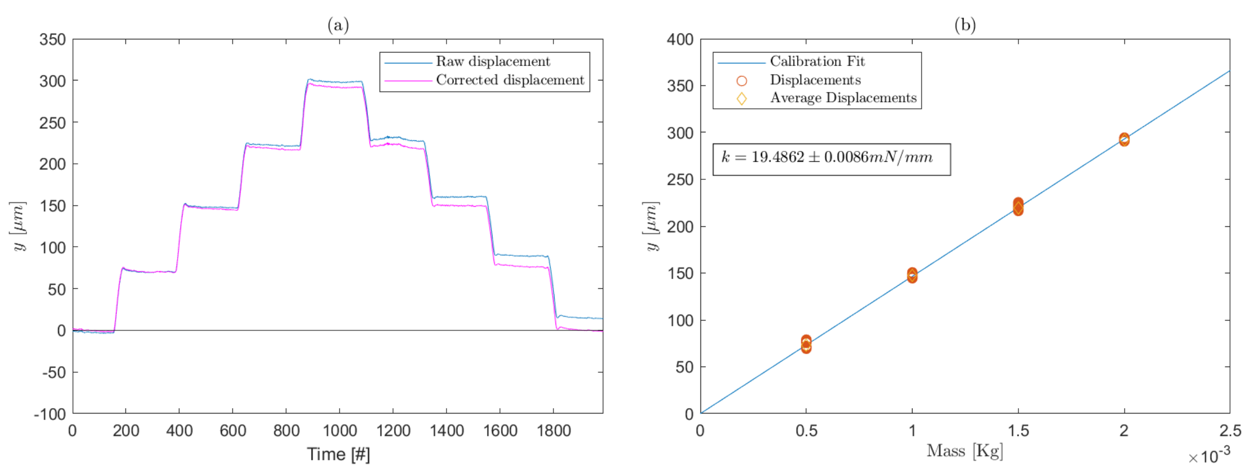

Fig. 7 Typical calibration output displacement.

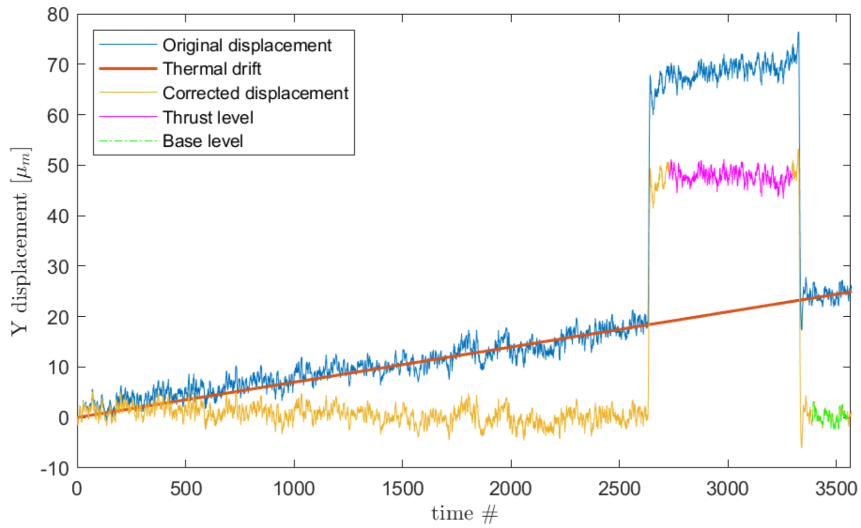

Fig. 8 Example of thrust measurement. The water cooling system was on during this measurement.

attached to an horizontal calibration arm of length L_{cal} = 200 mm, connected to the vertical arm of the TB. On the other side, the wire is wrapped around a spool connected to a stepper motor. Rotating the spool, the weights are lowered and in turn applied on the calibration arm one by one. Their weights apply a torque on the TB which is recorded as displacement by the displacement sensor. The displacement provided is equivalent to the one given by a thrust force F_{teq} at position L_t as $F_{teq} = F_{cal}L_{cal}/L_t$. In order to keep the wire always under tension, at least one weight is always applied on both of its sides. In this work, between 3 and 5 weights are applied in total during the calibration procedure. A typical calibration output displacement is shown in figure 7. For this particular case, the calibration factor κ found for the balance is κ = 66.88 mN/mm with a relative uncertainty of 0.044%. Once κ is obtained, the thrust F is simply obtained by equation 1.

$$F = \frac{L_{cal}}{L_t}\kappa y = ky \tag{1}$$

where y is the displacement due to the thrust force, k is the stiffness of the balance, L_t mm is the thrust vector distance from the vertical arm pivot point which has been measured to be L_t = 686.5 mm.

Calibrations are performed as well in-between thrust measurements to correct for drifts in calibration constant related to thermal effects. For this same reason the TB is equipped with a water cooling system which cools down the thruster mounting surface. The cooling system was used along the campaign at the cost of an increased noise level in the displacement measurements. Although these precautions were taken, the thermal drift due to the thruster temperature change visibly affected the barycenter position.

A thrust measurement is performed as follows: the desired $\dot{m}_p$ is set on the mass flow controller, the input power is set on the microwave generator to obtain the thruster ignition, the thruster is left on for the time necessary to reach the steady state, condition monitored using the thruster floating potential and the microwave reflection coefficient Γ^2. Then the power is cut and the mass flow as well. The reference for the TB displacement is thus taken. An example of thrust measurement is shown in figure 8.

III. Results

The performance measurements were done for low mass flow rates ($\dot{m}_p$ = 2 and 4sccm) and powers (P_T = 60 – 350W) since the thruster is expected to perform better in these conditions. The thrust balance has been used to directly evaluate the thrust F, and from it the specific impulse I_{sp} and thrust efficiency η_T.

The thrust results are shown in figure 9. For the analyzed cases, the thrust and I_{sp} are essentially linear with power. Repeated measurements under the same conditions yielded values within 5% of the reported ones. The thrust levels reached fall in the range 1 – 4 mN, and the I_{sp} in 300 – 1000 s. Similar thrust levels are found between 60 – 200 W for the mass flow rates evaluated, indicating a lower thrust efficiency for the 4 sccm case in that range.

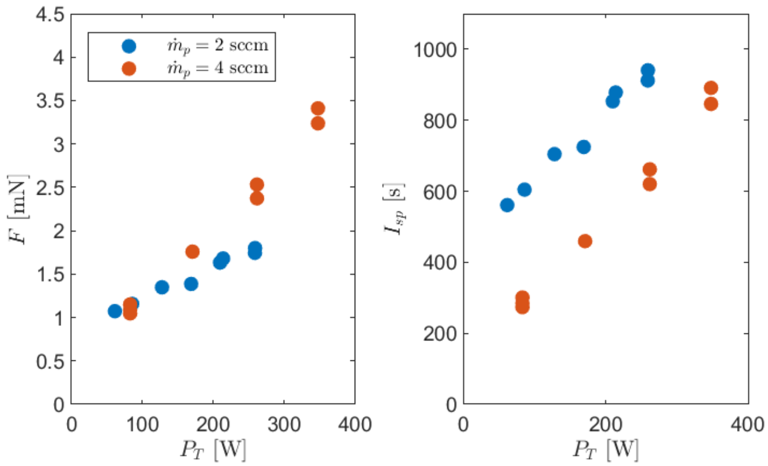

Fig. 9 Thrust and I_{sp} measurements.

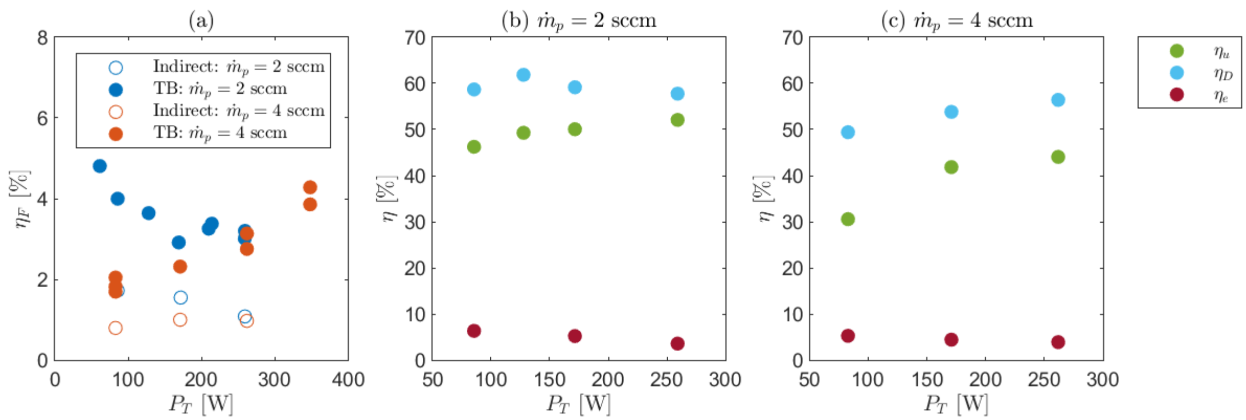

Fig. 10 (a) Comparison of the thrust efficiency obtained with direct and indirect thrust measurements. (b-c) partial efficiencies for $\dot{m}_p = 2 - 4$ sccm obtained using intrusive probes.

Thrust efficiency η_F is calculated from

$$\eta_F = \frac{F^2}{2\dot{m}_p P_T}, \tag{2}$$

and it is shown in figure 10a. The found efficiency levels are not far from what experienced by Crimi [13], ranging below 5% for the tested cases. Opposite trends with respect to P_T are found for the $\dot{m}_p = 2$ sccm and $\dot{m}_p = 4$ sccm cases, the first decreases with power, the second increases.

In order to explain the behaviour of η_F, and to gain further insight on the thruster performance and the loss mechanisms, partial efficiencies can be defined. Assuming plume axisymmetry, as in equation 3, the total plume current can be obtained by integrating the ion current density on an hemisphere, as measured with the FC at different angular positions (α) with respect to the thruster axis:

$$I_{tot} = 2\pi\rho^2 \int_0^{\pi/2} j_i(\alpha)\sin(\alpha)\, d\alpha, \tag{3}$$

The FC measurements also provide information on the plume divergence. The divergence angle can be found considering the portion of current directed in the axial direction,

$$\alpha_D = \cos^{-1}\left(\frac{I_{i,ax}}{I_{tot}}\right), \tag{4}$$

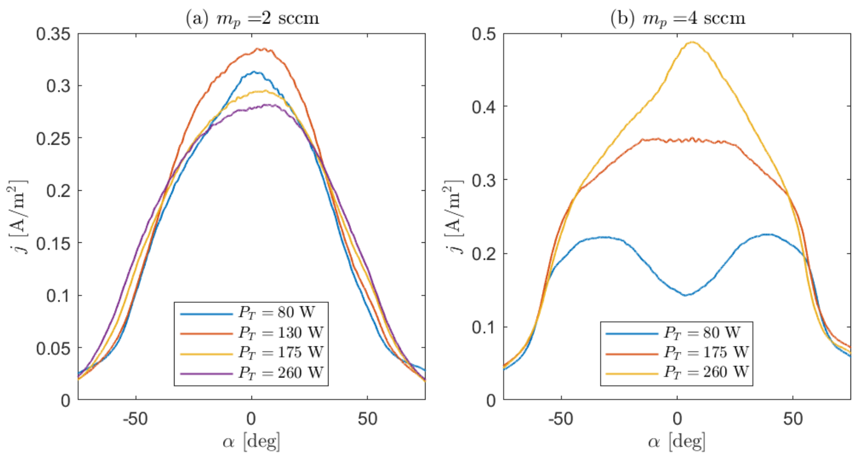

Fig. 11 Ion current densities profiles for the $\dot{m}_p$ = 2 sccm (a) and $\dot{m}_p$ = 4 sccm (b) for different power levels.

where I_{tot} and $I_{i,ax}$ are given by equations 3 and 5 respectively,

$$I_{i,ax} = 2\pi\rho^2 \int_0^{\pi/2} j_i(\alpha)\cos(\alpha)\sin(\alpha)\, d\alpha, \tag{5}$$

The utilization efficiency η_u, the plume divergence efficiency η_D and the energy efficiency η_e can be defined as in equations 6–8:

$$\eta_u = \frac{I_{tot} m_{Xe}}{\dot{m}_p e}, \tag{6}$$

$$\eta_D = \cos^2(\alpha_D) \tag{7}$$

$$\eta_e = \frac{\dot{m}_i v_i^2}{2P_T} = \frac{\dot{m}_p \eta_u v_i^2}{2P_T} \tag{8}$$

Notice that in order to take advantage of the experimental data obtained from the intrusive probes, some of these definitions differ from those used in other works of the group.

Referring to figure 10b, for the $\dot{m}_p$ = 2 sccm case, the plume divergence remains essentially constant around η_D = 60%, while the utilization ranges between 45 – 50% with an increasing trend with input power. Looking at the ion current density profiles for this mass flow rate (figure 11a) the ion current in the central peak increases going from P_T = 80 W to P_T = 130 W, increasing η_u and as well improving the divergence. Going to higher powers, however, increases the current produced at large angles at the peripheries of the plume, globally reducing the divergence efficiency.

Lower values of η_u and η_D are found for the $\dot{m}_p$ = 4 sccm case (figure 11b). Two distinct peaks are observed at large angles (hollow plume); these structures have been observed already in past works [18]. The formation of these peaks is believed to be linked to an increased microwave power coupled in proximity to the PC walls with respect to the channel axis. The increased neutral density due to the injection happening radially would increase the collisionality and thus the plasma density there, increasing in turn the power absorption in that region [24]. Rising the input power fills up the central gap, forming a central peak. Note that the plume current at large angles stays unaffected. Thus these trends explain the simultaneous increase of η_u and η_D.

Referring to figure 12, the considerations discussed above are confirmed by the emitted visible light observed looking at the thruster from the front. It is clear that increasing the mass flow rate moves the ionization/excitation processes from the center towards the thruster walls, finally leading to the creation of the observed hollow plume structure at 4 sccm. A similar behaviour is also obtained when the power is reduced at fixed mass flow rate, meaning that the amount of energy per electron is one of the driving forces for this trend. The higher electron temperature that can be found at large angles with respect to the axis (figure 15) further confirms that the microwave-plasma coupling is more pronounced close to the walls for the P_T = 80 W and 4 sccm case. Producing the majority of the plasma close to the thruster walls is certainly

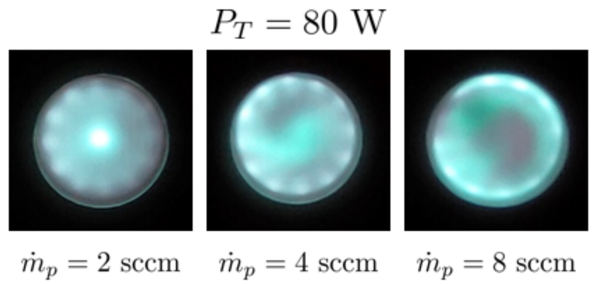

Fig. 12 Photo of the thruster viewed from the front during firing at $P_T = 80$ W and different levels of $\dot{m}_p$.

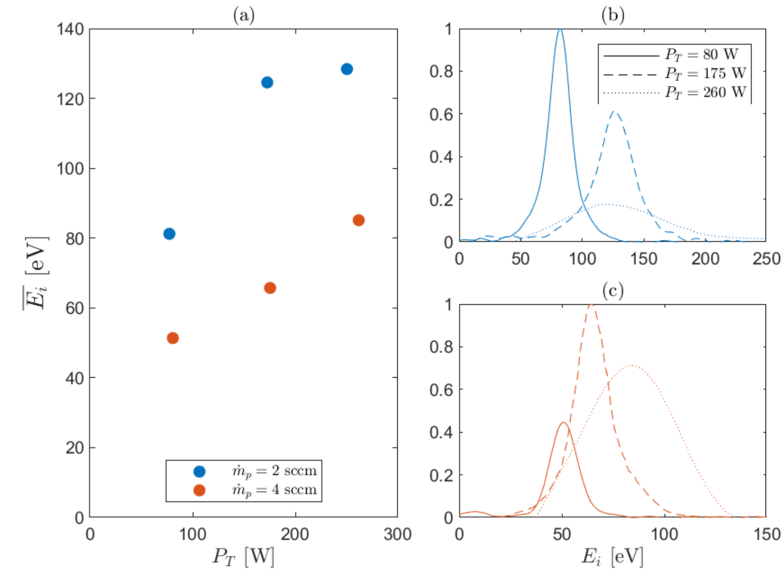

Fig. 13 Retarding Potential Analyzer (RPA) results for different working points. (a) Mean ion energy, (b-c) Ion energy distribution functions for $\dot{m}_p = 2 - 4$ sccm respectively.

detrimental, as it increases recombination providing an explanation to the the low energy efficiency. Furthermore also the divergence is increased consequently.

The energy efficiency (equation 8) takes into account inelastic collisional losses, power deposited on the thruster walls, and microwave power radiated away from the system if any. As it can be seen in figure 10b and 10c, this quantity is markedly low for the current setup. For both mass flow rate cases, there is a descending trend with power although this is more pronounced for the $\dot{m}_p = 2$ sccm case.

Referring to figure 13a, a maximum mean energy $\overline{E_i}$ of 130 eV and 85 eV was found for the $\dot{m}_p = 2$ sccm and $\dot{m}_p = 4$ sccm cases respectively. For both cases, the decrease in energy efficiency is linked to the fact that increasing P_T does not lead to an equivalent increase in $\overline{E_i}$. The $\dot{m}_p = 2$ sccm case appears to saturate the $\overline{E_i}$ explaining the more pronounced decrease in η_e, whereas the same does not happen yet for $\dot{m}_p = 4$ sccm. Looking at the ion energy distribution functions (figures 13b and 13c), it is evident that increasing input power also leads to an increase in ion temperature, suggesting that the ionization region is enlarging and therefore increasing the velocity spread of ions. Energies up to 200 eV are found for $\dot{m}_p = 2$ sccm.

Figure 14 shows an example of the plasma potential V_p trend for the case of $P_T = 175$ W and $\dot{m}_p = 2$ sccm, V_p reaches values around $V_p = 75$ V at $z = 100$ mm, comparing it to figure 13b leads to the conclusion that a non-negligible amount of ions are being produced within the plume or undergo collisions, similar conclusions can be obtained for the other working points as well.

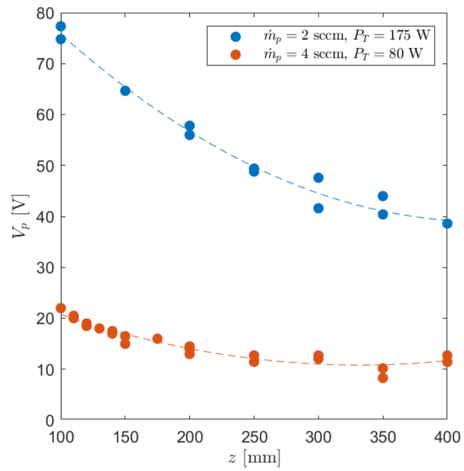

Fig. 14 Axial scan of the plasma potential V_p for two sample working points.

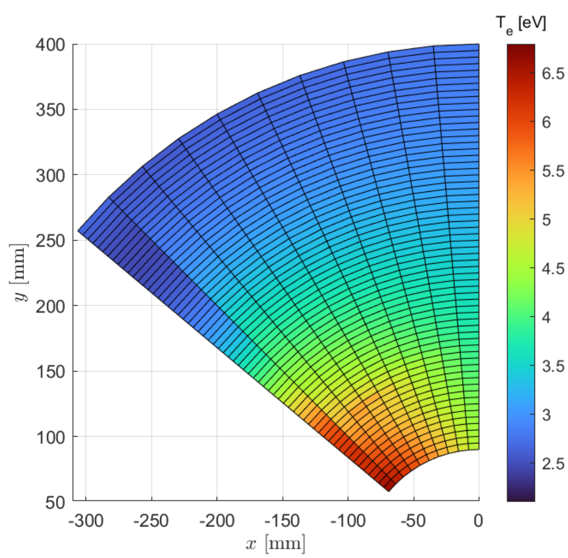

Fig. 15 Colormap of the electron temperature T_e for the $\dot{m}_p$ = 4 sccm and P_T = 80 W.

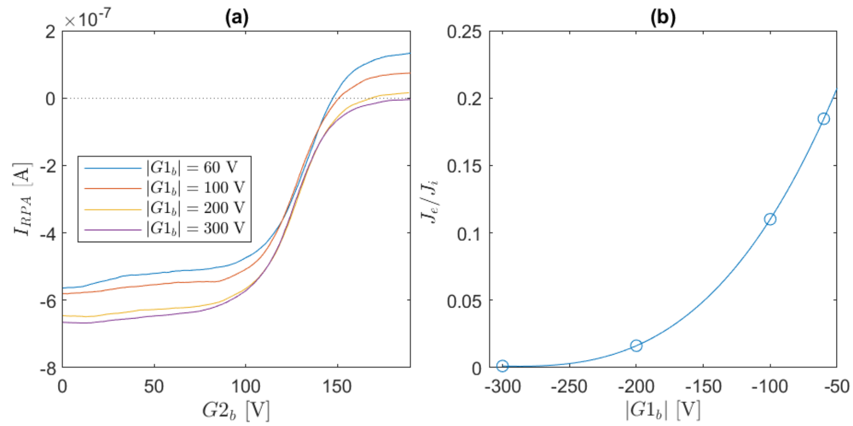

Fig. 16 $P_T = 175$ **W,** $\dot{m}_p = 2$ **sccm. (a) Examples of RPA scans for which the collected current does not saturate to 0 A at large bias of the swept Grid G2. (b) Values obtained for the ratio of electron current to ion current collected by the RPA collector electrode.**

Observe that:

$$\eta_F \approx \eta_u \eta_D \eta_e. \tag{9}$$

Equation 9 holds under the assumption that singly charged ions are the only species producing thrust and that they are mono-energetic, furthermore in equation 3 we have assumed plume axisymmetry which for this prototype is not necessarily guaranteed for all the working points. Coming back to figure 10a, a discrepancy of about 50% is found between the direct and indirect efficiency estimations. Excluding systematic errors in TB measurements, different sources could contribute to this problem: limitations in the axisymmetry and in the mono-energetic ion beam assumption, non-negligible electron or neutral momentum contributing to thrust, or the presence of double ions. Another source of error is as well brought by having considered α_D as a ratio of currents instead of powers.

Furthermore, RPA scans at different electron repelling grid (G1) voltages $G1_b$, have shown the presence of non-negligible collected electron currents if G1 is biased above the potential $G1_b = -300$ V, see figure 16. This fact may be associated with the presence of fast electrons with energies up to 300 eV. As found in past works[13], the presence of fast electrons is not something uncommon for ECR plasma thrusters where these electrons can be produced by the resonance. These were found as well by Peterschmitt [5], but they were observed only for the coaxial thruster version and not for the waveguide one. This fact might be due to the lower levels of power to mass flow rate ratio used in those tests or to a different microwave-plasma coupling mode. Evidences of larger fast electron energies and currents were seen for increasing power and reduced mass flow rate. Their presence has been measured on the thruster axis but whether they can be found at all α angles is still unknown. Looking at figure 16 it appears that the amount of fast electrons could account up to 10 % of the ion current collected by a FC biased at $V_{B-FC} = -120$ V (typical value used during the shown scans). Higher biasing values were not used since the FC I-V curve was not always showing a clear convergence region, effect probably linked to FC probe sheath expansion or increased SEE production due to the larger ion energies impacting the collector surface. Lastly, even if for the low power cases ($P_T = 80$ W) fast electrons were not seen, a discrepancy between the ion current collected with the FC and RPA has been found, the latter showing a current density in general $10 - 30\%$ larger than the FC. These effects combined introduce a significant error in the performed ion current measurements which resulted in the reduction of all the three partial efficiencies defined in equations 6-8.

IV. Conclusion

In this paper, the first direct thrust measurements on our waveguide ECR thruster prototype have been performed. The prototype was able to produce up to 3 mN of measured thrust. Two different trends were found for the thrust efficiency, descending with input power for the $\dot{m}_p = 2$ sccm case and ascending for the $\dot{m}_p = 4$ sccm, values below 5% were found for both cases. Intrusive probes results showed that for the low mass flow rate the trend is mainly explained by a decrease in energy efficiency, the higher power deposited is not converted efficiently into a larger ion acceleration. On the other hand, the increase of thrust efficiency for the $\dot{m}_p = 4$ sccm case is to be related with the increased divergence and utilization efficiency. However, a discrepancy between direct and indirect measurement was observed, the second being about 50% lower. Multiple could be the sources of this disagreement, one of the possibilities suggested is the presence of a considerable amount of fast electrons with energies up to 300eV, evidences of which were obtained with the use of an RPA. Finally, it has been shown that a consistent amount of ion current density can be measured at large angles from the axis (up to 50°) for the $\dot{m}_p = 4$ sccm case, we related the presence of these lateral peaks with strong ionization happening in proximity to the injector holes. This effect greatly increases the plume divergence and recombination with the thruster walls. Suggesting that the propellant injector design is essential for improving the thruster efficiency.

Acknowledgments

This work has been supported by the PROMETEO project, funded by the Comunidad de Madrid, under Grant reference Y2018/NMT-4750 PROMETEO-CM.

References

[1] Bathgate, S., Bilek, M., and Mckenzie, D., "Electrodeless plasma thrusters for spacecraft: a review," *Plasma Science and Technology*, Vol. 19, No. 8, 2017, p. 083001.

[2] Jarrige, J., Elias, P., Cannat, F., and Packan, D., "Characterization of a coaxial ECR plasma thruster," *44th AIAA Plasmadynamics and Lasers Conference, San Diego*, 2013.

[3] Cannat, F., Lafleur, T., Jarrige, J., Chabert, P., Elias, P., and Packan, D., "Optimization of a coaxial electron cyclotron resonance plasma thruster with an analytical model," *Physics of Plasmas*, Vol. 22, No. 5, 2015, p. 053503.

[4] Peterschmitt, S., and Packan, D., "Comparison of Waveguide Coupled and Coaxial Coupled ECRA Magnetic Nozzle Thruster using a Thrust Balance," 2019.

[5] Peterschmitt, S., and Packan, D., "Impact of the Microwave Coupling Structure on an Electron-Cyclotron Resonance Thruster," *Journal of Propulsion and Power*, Vol. 37, No. 6, 2021, pp. 806–815.

[6] Désangles, V., and D. Packan, J. J., "ECRA thruster advances, 30W and 200W prototypes latest performances," *IEPC 2022, Boston*, 2022.

[7] Stix, T. H., *Waves in plasmas*, Springer Science & Business Media, 1992.

[8] Bittencourt, J., *Fundamentals of plasma physics*, Springer, Berlin, Germany, 2004.

[9] Ahedo, E., and Merino, M., "Two-dimensional supersonic plasma acceleration in a magnetic nozzle," *Physics of Plasmas*, Vol. 17, No. 7, 2010, p. 073501.

[10] Merino, M., and Ahedo, E., "Magnetic Nozzles for Space Plasma Thrusters," *Encyclopedia of Plasma Technology*, Vol. 2, edited by J. L. Shohet, Taylor and Francis, 2016, pp. 1329–1351.

[11] Miller, D. B., and Gibbons, E. F., "Experiments with an electron cyclotron resonance plasma accelerator," *AIAA Journal*, Vol. 2, No. 1, 1964, pp. 35–41. https://doi.org/10.2514/3.2210, URL https://doi.org/10.2514/3.2210.

[12] Miller, D., Gibbons, E., and Gloersen, P., "Cyclotron resonance propulsion system," *Electric Propulsion Conference*, 1962, p. 2.

[13] Crimi, G., Eckert, A., and Miller, D., "Microwave Driven Magnetic Plasma Accelerator Studies (Cyclops)," Tech. rep., General Electric Company, Space Sciences Laboratory, Missile and Space Division, 1967.

[14] Sercel, J., "Electron-cyclotron-resonance (ECR) plasma acceleration," *AIAA 19th Fluid Dynamics, Plasma Dynamics and Lasers Conference*, 1987.

[15] Sercel, J., "Simple model of plasma acceleration in a magnetic nozzle," *21st International Electric Propulsion Conference*, Vol. 1, 1990.

[16] Sercel, J., "An experimental and theoretical study of the ECR plasma engine," Ph.D. thesis, California Institute of Technology, 1993.

[17] Inchingolo, M. R., Merino, M., and Navarro-Cavallé, J., "Hybrid PIC-Fluid Simulation of a Waveguide ECR Magnetic Nozzle Plasma Thruster," *Space Propulsion Conference 2021*, Association Aéronautique et Astronautique de France, March 17-19, 2021.

[18] Inchingolo, M., Navarro-Cavallé, J., and Merino, M., "Design and Plume Characterization of a Low-Power Circular Waveguide Coupled ECR Thruster," 5^{th} *International Workshop on Micropropulsion and CubeSats*, Toulouse (online), 2021.

[19] Pozar, D. M., *Microwave engineering*, John wiley & sons, 2011.

[20] Wijnen, M., "Diagnostic Methods for the Characterization of a Helicon Plasma Thruster," Ph.D. thesis, Universidad Carlos III de Madrid, Leganés, Spain, 2022.

[21] Lobbia, R. B., and Beal, B. E., "Recommended Practice for Use of Langmuir Probes in Electric Propulsion Testing," *Journal of Propulsion and Power*, Vol. 33, No. 3, 2017, pp. 566–581. https://doi.org/10.2514/1.B35531, URL https://doi.org/10.2514/1.B35531.

[22] Wijnen, M., Navarro-Cavallé, J., and Fajardo, P., "Mechanically amplified milli-newton thrust balance for direct thrust measurements of electric thrusters for space propulsion," *IEEE Transactions on Instrumentation and Measurement*, Vol. 70, 2021, p. 3505318.

[23] Polzin, K. A., Markusic, T. E., Stanojev, B. J., DeHoyos, A., and Spaun, B., "Thrust stand for electric propulsion performance evaluation," *Review of Scientific Instruments*, Vol. 77, No. 10, 2006, p. 105108.

[24] Sánchez-Villar, A., Zhou, J., Merino, M., and Ahedo, E., "Coupled plasma transport and electromagnetic wave simulation of an ECR thruster," *Plasma Sources Science and Technology*, Vol. 30, No. 4, 2021, p. 045005. https://doi.org/10.1088/1361-6595/abde20.